


# Systematic Matter and Binding-Energy Distributions from a Dispersive Optical Model Analysis

C. D. Pruitt<sup>1,\*</sup>, R. J. Charity<sup>1</sup>, L. G. Sobotka<sup>1,2</sup>, M. C. Atkinson<sup>2,†</sup> and W. H. Dickhoff<sup>2</sup>

<sup>1</sup>*Department of Chemistry, Washington University, St. Louis, Missouri 63130, USA*

<sup>2</sup>*Department of Physics, Washington University, St. Louis, Missouri 63130, USA*

 (Received 29 May 2020; revised 30 June 2020; accepted 22 July 2020; published 1 September 2020)

We present the first systematic nonlocal dispersive optical model analysis using both bound-state and scattering data of  $^{16,18}\text{O}$ ,  $^{40,48}\text{Ca}$ ,  $^{58,64}\text{Ni}$ ,  $^{112,124}\text{Sn}$ , and  $^{208}\text{Pb}$ . In all systems, roughly half the total nuclear binding energy is associated with the most-bound 10% of the total nucleon density. The extracted neutron skins reveal the interplay of asymmetry, Coulomb, and shell effects on the skin thickness. Our results indicate that simultaneous optical model fits of inelastic scattering and structural data on isotopic pairs are effective for constraining asymmetry-dependent nuclear structural quantities otherwise difficult to observe experimentally.

DOI: [10.1103/PhysRevLett.125.102501](https://doi.org/10.1103/PhysRevLett.125.102501)

**Introduction.**—Despite much investigation, the detailed behavior of individual nucleons in the nuclear ground state remains poorly understood. While many models can reproduce nuclear masses and charge radii across the nuclear chart, none can fully account for the *distribution*—in radial, energy, momentum, and angular-momentum space—of nucleons within the nuclear volume. For example, the precise location of excess neutrons in neutron-rich systems like  $^{48}\text{Ca}$  and  $^{208}\text{Pb}$  remains an open question, one that has received immense theoretical and experimental interest in recent years (thoroughly reviewed in [1]). The existence of “neutron skins,”  $\Delta r_{\text{np}}$ , on the surface of these and other stable nuclei is expected to correlate strongly with the density dependence of the nuclear symmetry energy, a major uncertainty in the neutron star equation of state [2–4]. Experimental difficulties in direct neutron skin measurements and uncertainty about the sensitivity of mean-field models to isovector quantities [5] make alternative approaches desirable. Ideally, a comprehensive model should not only reproduce integrated quantities (like the charge radius or total binding energy) but also specify how nucleons share momentum and energy, all while being realistic about the model uncertainty of its predictions [6].

A step toward these goals was the establishment of the dispersive optical model (DOM) [7], which formally extended traditional optical potentials to negative energies so that both reaction and structural information could be used to probe the nuclear potential (see the reviews of [8,9]). Previous DOM case studies have shown promise for exploring the systematics of nucleon behavior: for instance, generating trends in valence-shell spectroscopic factors as a function of asymmetry [10,11] and momentum [12], as well as extracting neutron skins [13–15]. However, each of these studies was narrow in scope: [12–14] examined only

a single Ca isotope each, while [10] included almost no bound-state information and thus was mute about matter and energy distributions. Cognizant of these challenges, we have completed a joint DOM analysis of the double and single closed-shell nuclei  $^{16,18}\text{O}$ ,  $^{40,48}\text{Ca}$ ,  $^{58,64}\text{Ni}$ ,  $^{112,124}\text{Sn}$ , and  $^{208}\text{Pb}$ , the first multinucleus treatment of nucleon matter and binding energy distributions in an optical model framework. For parameter optimization and uncertainty characterization, we relied on Markov Chain Monte Carlo (MCMC) sampling, an important improvement over techniques used for previous state-of-the-art optical potentials [16,17]. In all nine isotopes we examined, the small fraction of nucleon density far below the deepest single-particle energies (e.g., below  $-100$  MeV) was found to play a critical role for reproducing experimental binding energies. Before presenting these results, we first review salient elements of the DOM formalism.

**Relevant DOM formalism.**—Classical optical models describe nucleon-nucleus scattering with various forms of local phenomenological potentials defined only at positive energies [16–18]. In contrast, the DOM defines the complex, nucleon self-energy (or effective interaction),  $\Sigma^*(\alpha, \beta; E)$ , both above and below the Fermi energy. This potential-like object dictates nucleon behavior as it moves from state  $\alpha$  to state  $\beta$  in the nuclear medium at energy  $E$ , where  $\alpha, \beta$  denote complete sets of quantum numbers sufficient to specify the single-particle state. As in past DOM treatments [11–13,15], the self-energy domain was restricted to  $-300$  to  $200$  MeV with respect to the Fermi energy, a first-order relativistic correction was included, and only two-body forces were considered. The self-energy comprised three subcomponents:

$$\Sigma^*(\alpha, \beta; E) = \Sigma_{\text{st}}(\alpha, \beta) + \Sigma_{\text{im}}(\alpha, \beta; E) + \Sigma_{\text{dy}}(\alpha, \beta; E). \quad (1)$$

The “static” part of the self-energy  $\Sigma_{\text{st}}(\alpha, \beta)$  includes all real energy-independent contributions, taken here as a Hartree-Fock term evaluated at the Fermi energy, plus a spin-orbit term. The Fermi energy is defined via the ground-state energies for the  $A \pm 1$  systems:

$$\epsilon_F \equiv \frac{1}{2}[E_0^{A+1} + E_0^{A-1}]. \quad (2)$$

Each of the real subterms is parameterized with a Woods-Saxon form (or its derivative) coupled to a Gaussian non-locality. The energy-dependent imaginary component  $\Sigma_{\text{im}}(\alpha, \beta; E)$  consists of energy-dependent surface- and volume-associated terms at both positive and negative energies, again with nonlocal Woods-Saxons or their derivatives for radial dependence. Physically, these terms account for inelastic processes that require the most computational effort to recover in *ab initio* and shell-model treatments. To constrain these terms, the DOM instead relies on fitting flexible potential forms to experimental data. The “dynamic” (energy-dependent) real term  $\Sigma_{\text{dy}}(\alpha, \beta; E)$  is completely determined by integrating the imaginary term over the entire energy domain. It ensures that the self-energy obeys the required subtracted dispersion relation. The parameterization used is available in the companion article [19]; additional detail can be found in [20].

Following [21], the single-nucleon propagator is generated from the self-energy via the Dyson equation and the hole spectral function extracted from the propagator:

$$S_{lj}^h(\alpha; E) = \frac{1}{\pi} \text{Im}[G_{lj}(\alpha, \alpha; E)] \quad \text{for } E \leq \epsilon_F. \quad (3)$$

Here  $G$  and  $S$  are labeled with the (conserved) angular momentum  $l$  and total angular momentum  $j$ . Intuitively, the hole spectral function is the probability for removal of a particle with quantum numbers  $\alpha$  from an initial  $A$ -body system with ground-state energy  $E_0^A$ , leaving the residual  $(A-1)$ -body system with remaining energy  $E_0^A - E$ . Taking an explicit  $r$ -space basis for  $\alpha$ , the nucleon point density can be directly calculated from the hole spectral function:

$$\rho_{lj}(r) = \frac{1}{4\pi r^2} \int_{-\infty}^{\epsilon_F} (2j+1) S_{lj}^h(r; E) dE. \quad (4)$$

The total binding energy can be calculated per the Migdal-Galitsky rule, which is exact when only two-body interactions are included:

$$E_0^A = \frac{1}{2} \left[ \sum_{\alpha\beta} \langle \alpha | \hat{T} | \beta \rangle n_{\alpha\beta} + \sum_{\alpha} \int_{-\infty}^{\epsilon_F} S_{lj}^h(\alpha; E) E dE \right], \quad (5)$$

where  $\hat{T}$  is the kinetic energy operator appropriate for the single-particle basis and  $n_{\alpha\beta}$  is the one-body density

matrix. Three-body terms do not induce important corrections when energy densities are considered, supporting the use of Eq. (5) in DOM applications [22].

To constrain the self-energy, we applied nine sectors of experimental data for each nucleus: differential elastic-scattering cross sections, analyzing powers, reaction cross sections, total cross sections, binding energies, charge radii, charge densities, single-nucleon separation energies, and particle numbers. For fits on  $^{16,18}\text{O}$ ,  $^{40,48}\text{Ca}$ ,  $^{58,64}\text{Ni}$ , and  $^{112,124}\text{Sn}$ , all available data for each isotope pair were *simultaneously* fit using the same asymmetry-dependent potential; for  $^{208}\text{Pb}$ , only the  $^{208}\text{Pb}$  data were used. The new experimental isotopically resolved neutron total cross sections that motivated this work are reported in the companion experimental paper [19], which also includes a detailed comparison of DOM calculations to all experimental data, specifics of the MCMC implementation, and parameter estimates with uncertainties.

**Binding energies.**—Figure 1 shows the breakdown of particle density and binding energy for optimized fits of  $^{16,18}\text{O}$  and  $^{40,48}\text{Ca}$ . As in an independent-particle model, the vast majority of both proton and neutron density rests in the shells below the Fermi level. However, due to the imaginary potentials, a significant fraction, around 10%, appears in higher shells that would be fully unoccupied in a naive mean-field picture.

For both protons and neutrons, an outsized fraction of the binding energies comes from the most-bound levels. For example, the  $s_{1/2}$  states in  $^{16}\text{O}$  possess roughly 20% of the total nucleon density but almost 60% of the total binding energy. This is a consequence of the long tail of the hole spectral functions extending to extremely negative energies (more than 100 MeV below  $\epsilon_F$ ), far below the mean-field expectation. In both systems, the protons’ fraction of the total binding energy is slightly reduced (less bound) compared to that from the neutrons, a consequence of the Coulomb interaction. Overall, the substantial depletion of mean-field occupancies even in light systems (and the associated broadening of the bound nucleon spectral functions, as illustrated in [15]), is critical for achieving an average binding energy of 8 MeV/nucleon. We note that the binding energy distribution among shells that we recover for  $^{16}\text{O}$  agrees with that from the Brueckner-Hartree-Fock treatment of [23] and with general features of *ab initio* many-body calculations for nuclear matter [24].

Finally, we turn to the binding energy distributions for asymmetric  $^{18}\text{O}$  and  $^{48}\text{Ca}$  in Fig. 1. In these systems, the minority species (protons) experiences a deeper mean-field potential and a larger imaginary potential, increasing each proton’s relative share of the binding energy. For the majority species (neutrons), the effect is reversed: binding is reduced (less bound) for each shell compared to the symmetric system. For the valence  $d_{5/2}$  neutrons in  $^{18}\text{O}$  (in blue) and  $f_{7/2}$  neutrons in  $^{48}\text{Ca}$  (in orange), the contribution

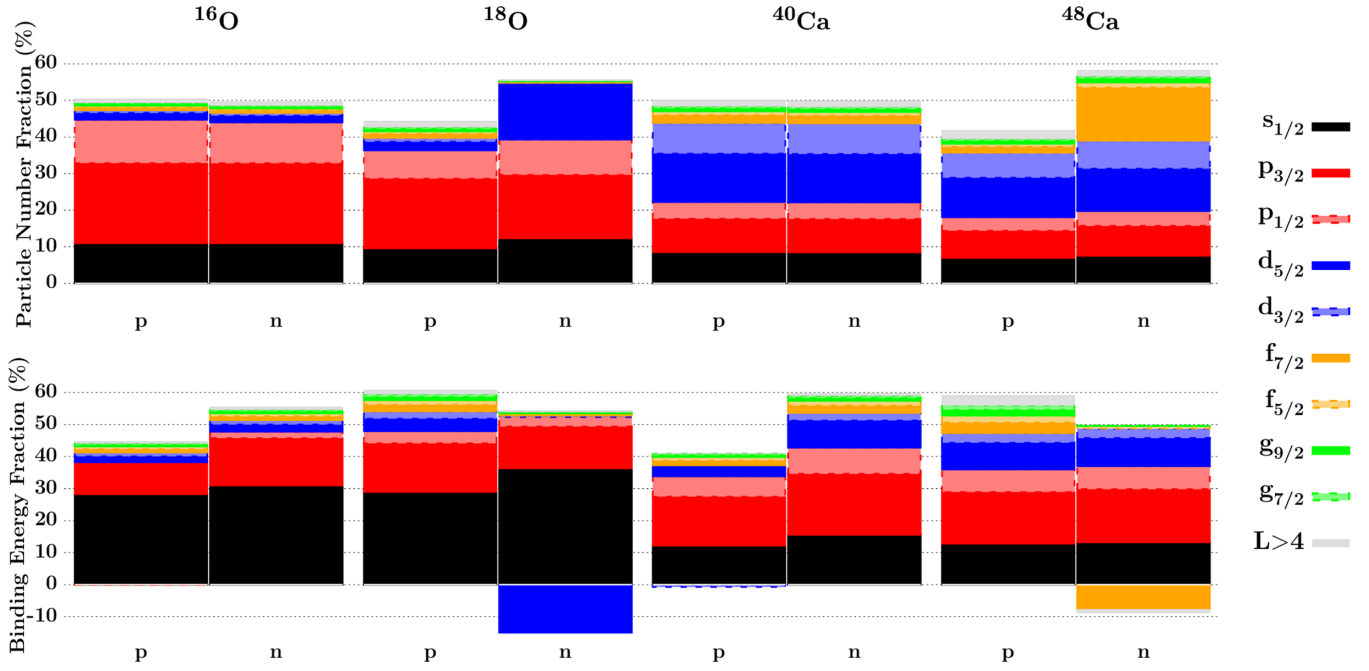


FIG. 1. DOM calculations of nucleon occupation and binding energy contributions as a function of angular momenta  $lj$  in  $^{16,18}\text{O}$  and  $^{40,48}\text{Ca}$ . The results shown are using the median posterior parameter values from MCMC sampling.

to the total binding is negative, that is, *unbinding*, because the bulk of their spectral density resides in quasiholes at or near the Fermi surface. This effect is more than compensated by the extra binding energy these valence neutrons induce in the *protons* compared to the symmetric case, such that the net effect is increased overall binding. These results are consistent with enhancement of short-range correlations among minority nucleons as identified by [25] in their investigation of nucleon high-momentum content as a function of asymmetry.

Figure 2 gives an  $lj$ -independent illustration of systematic behavior of the binding energy distribution. For each

system, the fraction of the total binding energy possessed by the most-bound 10% of the total nucleon density ( $BF_{10\%}$ ), regardless of quantum number, is plotted. The error bars indicate the 16th and 84th percentiles from the MCMC posterior distributions (the  $1\sigma$  region, if the posteriors are assumed to be Gaussian). For all systems analyzed here,  $BF_{10\%}$  exceeds 40%. To put this percentage in context, we performed an analogous “single-particle” calculation on  $^{40}\text{Ca}$  by artificially placing all spectral density for the  $s_{1/2}$  nucleons at their lowest single-particle eigenvalue. This scenario yields a  $BF_{10\%}$  of 31% for  $^{40}\text{Ca}$ , much lower than the median value of 48% from Fig. 2, demonstrating that the tiny nucleon density at extremely negative (deeply bound) energies makes an outsized contribution to overall binding.

To determine the relative effect of nuclear size and asymmetry on this quantity, we applied a linear model to the data,

$$BF_{10\%} = x_0 + A^{1/3}x_A + \frac{N-Z}{A}x_\alpha, \quad (6)$$

with  $N$ ,  $Z$ , and  $A$  the neutron, proton, and total nucleon numbers. MCMC sampling of this model gives parameter posterior values of  $x_0 = 36^{44}_{30}$ ,  $x_A = 4.1^{6.1}_{1.5}$ , and  $x_\alpha = 3^{31}_{-26}$ , where the 16th, 50th, and 84th percentile values are reported as  $50^{84}_{16}$ . Thus, the  $BF_{10\%}$  depends only weakly on the size of the system and is independent of asymmetry, indicating that, even in light nuclei, the bulk of the total binding comes from the few most-bound nucleons.

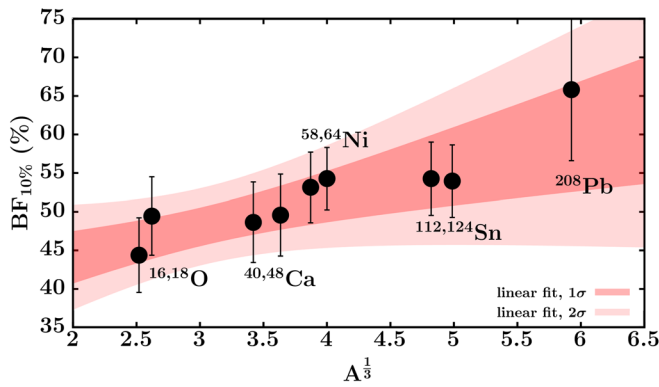


FIG. 2. Fraction of the total binding energy possessed by the most deeply bound 10% of the nucleon density for the isotopes studied in this work. The shaded regions indicate parametric uncertainty from fitting Eq. (6) to these data.

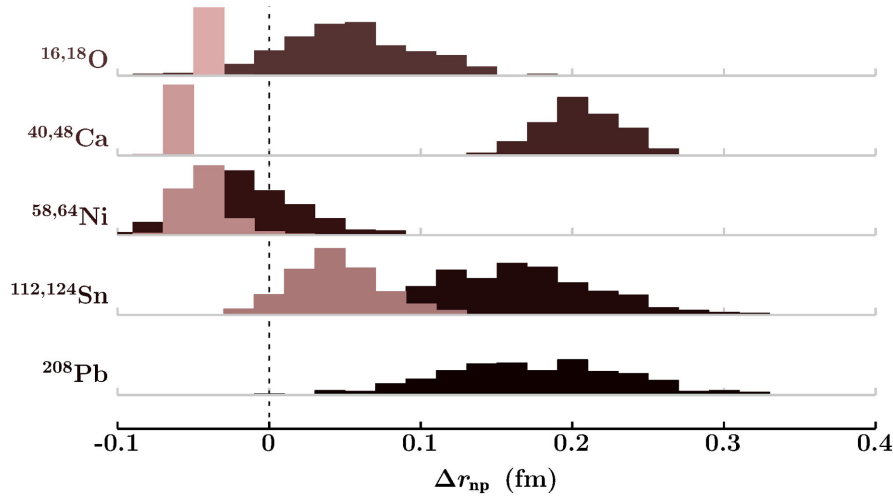


FIG. 3. Neutron skin probabilities via MCMC sampling for  $^{16,18}\text{O}$ ,  $^{40,48}\text{Ca}$ ,  $^{58,64}\text{Ni}$ ,  $^{112,124}\text{Sn}$ , and  $^{208}\text{Pb}$ . Each axis shows a single element. For elements with two isotopes histogrammed, the lighter isotope is shown using light bars, and the heavier isotope is shown with dark bars. The heights of each distribution have been arbitrarily rescaled to facilitate comparison.

*Neutron skins.*—The neutron skin

$$\Delta r_{\text{np}} \equiv r_{\text{rms}}(n) - r_{\text{rms}}(p) \quad (7)$$

was first identified as an important observable by Wilkinson over fifty years ago [26]. Neutron skins on neutron-rich nuclei are connected to other nuclear structural quantities, including the electric dipole polarizability, the location of the pygmy and giant dipole resonances, the density dependence of the symmetry energy, and the size of neutron stars [2,4,27–29].

The neutron skins extracted from the present work are shown in Fig. 3 and median values and uncertainties in Table I. We find that the degree of asymmetry,  $\alpha \equiv (N - Z)/A$ , correlates strongly ( $r = 0.89$ ) with the median skin thicknesses. If a simple linear dependence in  $\alpha$  is assumed, extrapolation from the  $^{58,64}\text{Ni}$  skins gives a  $^{56}\text{Ni}$  skin thickness of  $-0.04 \pm 0.03$  fm. A similar calculation with  $^{112,124}\text{Sn}$  yields a  $^{100}\text{Sn}$  skin thickness of  $-0.07 \pm 0.06$  fm. In the symmetric systems  $^{16}\text{O}$  and  $^{40}\text{Ca}$ , Coulomb repulsion nudges proton density outward from the core, resulting in a small negative neutron skin (that is, a proton skin). Again assuming the linear dependence of this Coulomb effect, extrapolation from  $^{16}\text{O}$  and  $^{40}\text{Ca}$  gives neutron skins of  $-0.07 \pm 0.02$  fm for  $^{56}\text{Ni}$  and  $-0.12 \pm 0.04$  fm for  $^{100}\text{Sn}$ , slightly more negative than, but in keeping with, the linear extrapolation from  $^{58,64}\text{Ni}$

and  $^{112,124}\text{Sn}$ . Besides Coulomb and asymmetry-dependent effects, the large  $^{48}\text{Ca}$  median skin of 0.22 fm and near-zero median  $^{64}\text{Ni}$  skin of  $-0.01$  fm show the importance of shell effects for certain systems (cf. with  $^{208}\text{Pb}$  results of [15]). To wit, most of the excess neutrons in  $^{48}\text{Ca}$  and  $^{64}\text{Ni}$  enter the neutron  $f_{7/2}$  and neutron  $p_{3/2}$  shells, respectively, as seen in Fig. 1 for  $^{48}\text{Ca}$ . The mean radius of the  $f_{7/2}$  shell is larger than the deeper shells; thus, when neutron density is added, the size grows rapidly. In  $^{64}\text{Ni}$ , the neutron  $1p_{3/2}$  rms radius is closer to the overall  $r_{\text{rms}}(n)$  of  $^{58}\text{Ni}$ , so the additional neutrons of  $^{64}\text{Ni}$  do little to grow the skin thickness.

For  $^{18}\text{O}$ , the mirror-nuclei logic of [30] can be applied to cross-check our skin value. Assuming isospin symmetry, the difference between the  $^{18}\text{Ne}$  and  $^{18}\text{O}$  charge radii is a good proxy for the  $^{18}\text{O}$  neutron skin thickness. Per [31], the charge radius difference between  $^{18}\text{Ne}$  and  $^{18}\text{O}$  is  $0.20 \pm 0.01$  fm. Before comparing this proxy value with the neutron skin of  $^{18}\text{O}$ , Coulomb and deformation corrections must be applied. First, due to the Coulomb force, the proton density of  $^{18}\text{Ne}$  extends further than the neutron density of  $^{18}\text{O}$ . We estimate the magnitude of this proton density extension in  $^{18}\text{Ne}$  as 0.03 fm, or 25% larger than the difference between the proton and neutron distributions of  $^{16}\text{O}$ , due to the 25% larger proton number of  $^{18}\text{Ne}$ . Subtracting 0.03 fm from the  $^{18}\text{Ne}$ - $^{18}\text{O}$  radius difference yields 0.17 fm. Second, because  $^{18}\text{Ne}$  is more deformed

TABLE I. Neutron skins ( $\Delta r_{\text{np}}$ ), in fm, from this work. The 16th, 50th, and 84th percentile values of the skin distribution are reported as  $50^{84}_{16}$ .

$^{16}\text{O}$	$^{18}\text{O}$	$^{40}\text{Ca}$	$^{48}\text{Ca}$	$^{58}\text{Ni}$	$^{64}\text{Ni}$	$^{112}\text{Sn}$	$^{124}\text{Sn}$	$^{208}\text{Pb}$
$-0.025^{0.023}_{-0.027}$	$0.06^{0.11}_{0.02}$	$-0.051^{0.048}_{-0.055}$	$0.22^{0.24}_{0.19}$	$-0.03^{0.02}_{-0.05}$	$-0.01^{0.03}_{-0.04}$	$0.05^{0.08}_{0.02}$	$0.17^{0.23}_{0.12}$	$0.18^{0.25}_{0.12}$



( $\beta_2 = 0.68$ ) than  $^{18}\text{O}$  ( $\beta_2 = 0.37$ ) [32], any deformation correction will further reduce this proxy value. Absent a clean way to generate this correction, the proxy can only be taken as an *upper limit* on the  $^{18}\text{O}$  neutron skin. Our skin prediction for  $^{18}\text{O}$  of  $0.06_{0.02}^{0.11}$  fm is compatible with the upper limit of 0.17 fm provided by this heuristic symmetry argument.

Our median results for  $^{48}\text{Ca}$  (0.22 fm) and  $^{208}\text{Pb}$  (0.18 fm) are somewhat smaller than those from previously mentioned DOM case studies but with significant uncertainty range overlap [14,15]. We attribute the variation to differences in the potential parameterization, our joint fitting of isotope pairs, and our MCMC optimization approach. The values reported here for  $^{48}\text{Ca}$  and  $^{208}\text{Pb}$  are quite close to those from recent experimental studies [33–35] and from the relativistic density functional model FSUGold as reported in [1]. However, our predicted skin range for  $^{48}\text{Ca}$  differs significantly from the recent coupled-cluster-based prediction of 0.12–0.15 fm from [36], a discrepancy we hope the proposed Calcium Radius Experiment will resolve. Lastly, the median skins we recover for  $^{112,124}\text{Sn}$  (0.05 and 0.17 fm, respectively) are almost identical to those extracted by [37] (0.06 and 0.18 fm, respectively) from analysis of 295 MeV proton elastic scattering on Sn isotopes.

**Conclusions.**—Using a newly generalized version of the DOM, we performed the first systematic DOM analysis across nine isotopes from  $A = 16$  to  $A = 208$  to extract matter and binding-energy distributions. Using MCMC with model discrepancy terms and joint fitting of multiple isotopes, we generated realistic uncertainties for all potential parameters and extracted quantities. Our results quantitatively indicate how asymmetry, Coulomb, and shell effects contribute to neutron skin generation and drive a disproportionate share of the total binding energy to the deepest nucleons. Using simple trends in  $^{16}\text{O}$ ,  $^{40}\text{Ca}$ ,  $^{58,64}\text{Ni}$ , and  $^{112,124}\text{Sn}$ , we estimate the  $^{56}\text{Ni}$  neutron skin as between  $-0.04$  and  $-0.07$  fm and between  $-0.07$  and  $-0.12$  fm for  $^{100}\text{Sn}$ . Our skin thickness for  $^{18}\text{O}$  agrees with the mirror-nucleus upper bound expectation, and the agreement of our  $^{48}\text{Ca}$ ,  $^{112,124}\text{Sn}$ ,  $^{208}\text{Pb}$  skin thicknesses with recent external predictions augers well for a future truly global DOM treatment.

This work is supported by the U.S. Department of Energy, Office of Science, Office of Nuclear Physics under Award No. DE-FG02-87ER-40316 and by the U.S. National Science Foundation under Grant Nos. PHY-1613362 and PHY-1912643. The work was performed in part under the auspices of the U.S. Department of Energy by Lawrence Livermore National Laboratory under Contract No. DE-AC52-07NA27344. C. D. P. acknowledges support from the U.S. Department of Energy, National Nuclear Security Administration, under Award No. DE-NA0003841, the Center for Excellence in Nuclear Training and University-based Research (CENTAUR).

\*Corresponding author.

pruitt9@llnl.gov

Present Address: Lawrence Livermore National Laboratory, Livermore, California.

†Present Address: TRIUMF, Vancouver, Canada.

- [1] M. Thiel, C. Sienti, J. Piekarewicz, C. J. Horowitz, and M. Vanderhaegen, *J. Phys. G* **46**, 093003 (2019).
- [2] F. J. Fattoyev and J. Piekarewicz, *Phys. Rev. C* **86**, 015802 (2012).
- [3] J. Piekarewicz, B. K. Agrawal, G. Colo, W. Nazarewicz, N. Paar, P. G. Reinhard, X. Roca-Maza, and D. Vretenar, *Phys. Rev. C* **85**, 041302(R) (2012).
- [4] X. Viñas, M. Centelles, X. Roca-Maza, and M. Warda, *Eur. J. Phys. A* **50**, 27 (2014).
- [5] R. Furnstahl, *Nucl. Phys.* **A706**, 85 (2002).
- [6] The Editors, *Phys. Rev. A* **83**, 040001 (2011).
- [7] C. Mahaux and R. Sartor, *Adv. Nucl. Phys.* **20**, 1 (1991).
- [8] W. H. Dickhoff, R. J. Charity, and M. H. Mahzoon, *J. Phys. G* **44**, 033001 (2017).
- [9] W. H. Dickhoff and R. J. Charity, *Prog. Part. Nucl. Phys.* **105**, 252 (2019).
- [10] J. M. Mueller, R. J. Charity, R. Shane, L. G. Sobotka, S. J. Waldecker, W. H. Dickhoff, A. S. Crowell, J. H. Esterline, B. Fallin, C. R. Howell, C. Westerfeldt, M. Youngs, B. J. Crowe, and R. S. Pedroni, *Phys. Rev. C* **83**, 064605 (2011).
- [11] M. C. Atkinson and W. H. Dickhoff, *Phys. Lett. B* **798**, 135027 (2019).
- [12] M. C. Atkinson, H. P. Blok, L. Lapidás, R. J. Charity, and W. H. Dickhoff, *Phys. Rev. C* **98**, 044627 (2018).
- [13] M. H. Mahzoon, R. J. Charity, W. H. Dickhoff, H. Dussan, and S. J. Waldecker, *Phys. Rev. Lett.* **112**, 162503 (2014).
- [14] M. H. Mahzoon, M. C. Atkinson, R. J. Charity, and W. H. Dickhoff, *Phys. Rev. Lett.* **119**, 222503 (2017).
- [15] M. C. Atkinson, M. H. Mahzoon, M. A. Keim, B. A. Bordelon, C. D. Pruitt, R. J. Charity, and W. H. Dickhoff, *Phys. Rev. C* **101**, 044303 (2020).
- [16] R. L. Varner, W. J. Thompson, T. L. McAbee, E. J. Ludwig, and T. B. Clegg, *Phys. Rep.* **201**, 57 (1991).
- [17] A. J. Koning and J. P. Delaroche, *Nucl. Phys.* **A713**, 231 (2003).
- [18] F. J. Becchetti and G. Greenlees, *Phys. Rev.* **182**, 1190 (1969).
- [19] C. D. Pruitt *et al.*, companion paper, *Phys. Rev. C* **102**, 034601 (2020).
- [20] C. D. Pruitt, Ph.D. Thesis, Washington University in St Louis, 2019.
- [21] W. H. Dickhoff and D. Van Neck, *Many-Body Theory Exposed!*, 2nd ed. (World Scientific, Singapore, 2008).
- [22] M. C. Atkinson, W. H. Dickhoff, M. Piarulli, A. Rios, and R. B. Wiringa, [arXiv:2001.07231](https://arxiv.org/abs/2001.07231).
- [23] H. Mütter, A. Polls, and W. H. Dickhoff, *Phys. Rev. C* **51**, 3040 (1995).
- [24] B. E. Vonderfecht, W. H. Dickhoff, A. Polls, and A. Ramos, *Nucl. Phys.* **A555**, 1 (1993).
- [25] O. Hen, E. Piasetzky, and L. B. Weinstein, *Phys. Rev. C* **85**, 047301 (2012).
- [26] D. H. Wilkinson, *Comments Nucl. Part. Phys.* **1**, 80 (1967), <https://inspirehep.net/literature/1381641>.
- [27] B. A. Brown, *Phys. Rev. Lett.* **85**, 5296 (2000).
- [28] Z. Zhang, Y. Lim, J. W. Holt, and C. M. Ko, *Phys. Lett. B* **777**, 73 (2018).

- 
- [29] S. Typel and B. A. Brown, *Phys. Rev. C* **64**, 027302 (2001).
  - [30] B. A. Brown, *Phys. Rev. Lett.* **119**, 122502 (2017).
  - [31] I. Angeli and K. Marinova, *At. Data Nucl. Data Tables* **99**, 69 (2013).
  - [32] NUDAT2 database, <https://www.nndc.bnl.gov/nudat2>, Accessed 2020-4-28.
  - [33] J. Zenihiro, H. Sakaguchi, S. Terashima, T. Uesaka, G. Hagen, M. Itoh, T. Murakami, Y. Nakatsugawa, T. Ohnishi, H. Sagawa, H. Takeda, M. Uchida, H. P. Yoshida, S. Yoshida, and M. Yosoi, [arXiv:1810.11796](https://arxiv.org/abs/1810.11796).
  - [34] C. M. Tarbert *et al.* (Crystal Ball at MAMI and A2 Collaboration), *Phys. Rev. Lett.* **112**, 242502 (2014).
  - [35] J. Zenihiro, H. Sakaguchi, T. Murakami, M. Yosoi, Y. Yasuda, S. Terashima, Y. Iwao, H. Takeda, M. Itoh, H. P. Yoshida, and M. Uchida, *Phys. Rev. C* **82**, 044611 (2010).
  - [36] G. Hagen, A. Ekström, C. Forssén, G. R. Jansen, W. Nazarewicz, T. Papenbrock, K. A. Wendt, S. Bacca, N. Barnea, B. Carlsson, C. Drischler, K. Hebeler, M. Hjorth-Jensen, M. Miorelli, G. Orlandini, A. Schwenk, and J. Simonis, *Nat. Phys.* **12**, 186 (2016).
  - [37] S. Terashima, H. Sakaguchi, H. Takeda, T. Ishikawa, M. Itoh, T. Kawabata, T. Murakami, M. Uchida, Y. Yasuda, M. Yosoi, J. Zenihiro, H. P. Yoshida, T. Noro, T. Ishida, S. Asaji, and T. Yonemura, *Phys. Rev. C* **77**, 024317 (2008).